Remote Sensing of Environment 174 (2016) 233–243

Contents lists available at ScienceDirect

Remote Sensing of Environment

journal homepage: www.elsevier.com/locate/rse

Remote sensing of the surface urban heat island and land architecture in Phoenix, Arizona: Combined effects of land composition and configuration and cadastral–demographic–economic factors

Xiaoxiao Li [a,*], Wenwen Li [b], A. Middel [a,b], S.L. Harlan [c], A.J. Brazel [a,b], B.L. Turner II [a,b,d]

[a] Julie Ann Wrigley Global Institute of Sustainability, Arizona State University, Tempe, AZ 85287-5402, United States
[b] School of Geographical Sciences & Urban Planning, Arizona State University, Tempe, AZ 85287-5302, United States
[c] Department of Health Sciences and Department of Sociology, Northeastern University, Boston, Massachusetts, 02115, United States
[d] School of Sustainability, Arizona State University, Tempe, AZ 85287-5502, United States

ARTICLE INFO

Article history:
Received 20 October 2014
Received in revised form 5 November 2015
Accepted 15 December 2015
Available online 29 December 2015

Keywords:
Land architecture
Surface urban heat island
Land surface temperature
Land cover
Spatial pattern

ABSTRACT

This study seeks to determine the role of land architecture—the composition and configuration of land cover—as well as cadastral–demographic–economic factors on land surface temperature (LST) and the surface urban heat island effect of Phoenix, Arizona. It employs 1 m National Agricultural Imagery Program data of land-cover with 120 m Landsat-derived land surface temperature, decomposed to 30 m, a new measure of configuration, the normalized moment of inertia, and U.S. Census data to address the question for two randomly selected samples comprising 523 and 545 residential neighborhoods (census blocks) in the city. The results indicate that, contrary to most other studies, land configuration has a stronger influence on LST than land composition. In addition, both land configuration and architecture combined with cadastral, demographic, and economic variables, capture a significant amount of explained variance in LST. The results indicate that attention to land architecture in the development of or reshaping of neighborhoods may ameliorate the summer extremes in LST.

1. Introduction

The urban heat island (UHI) effect refers to the higher air and surface temperature in urban areas compared to that of the surrounding rural hinterland, generated by high levels of near surface energy emission, solar radiation absorption of ground objects, and often, low levels of evapotranspiration in cities (Buyantuyev & Wu, 2010; Oke, 1982, 1997; Rizwan, Dennis, & Liu, 2008). The UHI of large cities has increased substantially since the middle of the 20th century (Akbari, Pomerantz, & Taha, 2001; Oke, 1976; Stone, 2007), with urban conglomerations generating modeled and observed changes in regional temperatures (Georgescu, Moustaoui, Mahalov, & Dudhia, 2011; He, Liu, Zhuang, Zhang, & Liu, 2007; Kalnay & Cai, 2003; Li, Wang, Shen, & Song, 2004). Extensively examined, the UHI draws increasing attention owing to its effects on energy and water consumption, human health, environmental (ecosystem) services, especially in the context of global warming (e.g. Gober, Kirkwood, Balling, Ellis, & Deitrick, 2009; Harlan, Brazel, Prashad, Stefanov, & Larsen, 2006; Harlan, Declet-Barreto, Stefanov, & Petitti, 2013; Hondula, Vanos, & Gosling, 2013; Hondula et al., 2012). For these and other reasons, attention to the means to mitigate the UHI effect have garnered considerable attention, especially through model simulations (e.g. Golany, 1996; Sailor, 1995), but increasingly through the use or remote sensing data that permit novel assessments (e.g., Zhou, Huang, & Cadensasso, 2011).

Remote sensing technology has been a boon to the study of the UHI in at least two fundamental ways: [1] direct observation of land surface thermal radiance converted to land surface temperature to address the Surface UHI (SUHI) (e.g. Lo, Qiattrochi, & Luvall, 1997; Streutker, 2002); and [2] direct spatial linkages of ground features, both their vertical dimensions and patterns, to land surface temperature at fine spatial resolutions (e.g. Arnfield, 2003; Buyantuyev & Wu, 2010; Chow, Chuang, & Gober, 2012; Nichol, 1996; Unger, 2004). To date, this research has focused on the relationship between land surface temperature (LST) and particular land-cover types (or land composition) (e.g. Chow & Brazel, 2012; Li, Song, Cao, Meng, & Wu, 2011; Middel, Häb, Brazel, Martin, & Guhathakurta, 2014; Stone & Rodgers, 2001; Zheng, Myint, & Fan, 2014; Zhou et al., 2011), and between spatial thermal patterns and social economic factors (Buyantuyev & Wu, 2010; Harlan et al., 2006; Hondula et al., 2013; Huang, Zhou, & Cadenasso, 2011; Jenerette, Harlan, Stefanov, & Martin, 2011). Recently, however, attention to land system architecture (Turner, Janetos, Verburg, & Murray, 2013)—the composition and configuration (e.g., size, shape, patterns, and connectivity) of the urban land cover—on SUHI has been examined in regard to possible UHI mitigation strategies (Chen, Zhao, Li, & Yin,

* Corresponding author.
E-mail address: xiaoxia4@asu.edu (X. Li).

http://dx.doi.org/10.1016/j.rse.2015.12.022
0034-4257/

2006; Connors, Galletti, & Chow, 2013; Li, Zhou, Quyang, & Zheng, 2012; Li et al., 2013b; Zhou et al., 2011).

Briefly summarizing, this research informs us that increasing greenspace, water, and skyview (open area ventilation) tend to ameliorate the UHI effect, while dark-colored impervious surfaces tend to amplify it, with larger impacts on nighttime temperatures (e.g. Chow & Brazel, 2012; Li et al., 2011; Maimaitiyiming et al., 2014; Weng, Lu, & Schubring, 2004; Xian & Crane, 2006; Zheng et al., 2014; Zhou, Qian, Li, Li, & Han, 2014). These relationships tend to hold across different urban areas and environments, but vary in magnitude diurnally and seasonally. Specific linkages to human outcomes demonstrate that UHI impacts tend to be registered most highly among those parts of city that have dense occupation with low levels of shade, either from buildings or trees, and greenspaces. These conditions, at least in the U.S. cities examined, tend to be related to lower levels of income, often linked to neighborhoods dominated by certain ethnic groups (Buyantuyev & Wu, 2010; Harlan et al., 2006; Hondula et al., 2012; Jenerette et al., 2007, 2011). Finally, the land architecture of urban areas, from the parcel to larger levels of assessment, has been hypothesized to amplify or ameliorate ecosystem services, such as those related to SUHI effects (Turner et al., 2013). Nascent research suggests that, controlling for land composition, edge and patch densities, landscape shape index, and fractal dimensions (FRAGSTAT metrics) of land covers hold significant consequences for land surface temperatures (Buyantuyev & Wu, 2010; Connors et al., 2013; Li et al., 2011; Li et al., 2012; Middel, Brazel, Kaplan, & Myint, 2012; Middel et al., 2014; Stone & Rodgers, 2001; Zhang, Odeh, & Ramadan, 2013; Zhang, Zhong, Feng, & Wang, 2009; Zhou et al., 2011).

Our study follows from but extends these lines of research. It seeks to determine if LST among residential neighborhoods during the summer season, specifically June, is related to the land architecture and certain cadastral, demographic, and socioeconomic characteristics of the neighborhoods in the metropolitan area of Phoenix, AZ. We employ fine resolution spatial data and a compactness pattern measure—the normalized moment of inertia—applied for the first time in land architecture assessments. We test the following hypotheses drawn from or implied in the body of research reviewed above:

[1] [1] *The composition and configuration* (i.e., *land architecture*) *of land-cover types affect summer daytime LST and thus the SUHI*. Research to date has yet to explicate adequately the configuration dimensions of multiple land covers on SUHI.

[2] [2] *Land composition is more strongly related to summer daytime LST than configuration*. Most of the research results to date, typically using FRAGSTATS metrics, indicate the stronger role of composition, or area of land covers, on the SUHI.

[3] [3] *Land architecture has more impact on summer daytime LST than do cadastral–demographic–socioeconomic factors*. Some research implies that these factors and land architecture may be linked, but assessing their relative roles has yet to be examined fully. In our study, cadastral data provide information on parcel size, which are used as ancillary data for the economic dimension in question.

2. Study area, data, and methods

2.1. Study area

The City of Phoenix, AZ, is the center of an expansive metropolitan area located on the northern edge of the Sonoran Desert (Fig. 1). June maximum daily temperatures average 40 °C, with the highest recorded temperature reaching 48.3 °C (Middel et al., 2012). Temperatures are amplified by the UHI effect, especially in regard to an enlarged minimum night time temperature (Chow et al., 2012; Hawkins, Brazel, Stefanov, Bigler, & Saffell, 2004; Stabler, Martin, & Brazel, 2005). This effect has been triggered by the massive growth in the metropolis. Since the middle of the 20th century, there have been major increases in the area of impervious surface and numbers of residential parcels and neighborhoods with different levels of vegetation and bare soil (including rock and desert surfaces). Residential landscape composition—variations of turf lawns to xeric- and desert-scapes—are associated with the period of development, rules of Home Owner Associations (HOAs), and income levels, among other factors (Chow & Brazel, 2012; Kane, Connors, & Galletti, 2014; Larson, White, Gober, Harlan, & Wutich, 2009b; Sha & Tian, 2010; Shrestha, York, Boone, & Zhang, 2012; Turner & Ibes, 2011). For the most part, the presence of vegetation and open greenspaces beyond residential parcels (e.g., parks and golf courses) varies across the city, with lower levels of both apparently related to lower income and Hispanic neighborhoods in Phoenix proper (Harlan et al., 2006; Jenerette et al., 2011).

2.2. Data and methods

2.2.1. Parcel and neighborhood selection

This study draws on residential census blocks (Fig. 1), our surrogate for neighborhoods, composed primarily, but not exclusively, of single family residential parcels and for which cadastral data provide land-use information for each parcel. Two random samples (A and B) were employed in order to verify the results of the exercise, and each sample was drawn by the same method (Fig. 1). The Create Random Points function in the GIS software ArcMap selected 1000 single family residential parcels (0.2% of such parcels in the city) for both samples. To ensure spatial independence, both samples were reduced by applying a distance filter in which each parcel had to be at least 1000 m from the others. The census block (neighborhood) for each parcel was identified, and another distance filter was applied: each census block had to be at least 500 m from one another. This sampling and filtering procedure yielded 21,505 and 24,167 single family parcels that are distributed over 523 and 545 census blocks, respectively, across the city. The parcel and census block selection outcomes are provided in Table 1 and the distributions of the A and B sample census blocks are mapped in Fig. 1.

At least two issues are noteworthy in our sample. First, parts of the metropolitan area with the highest SUHI were excluded from consideration because they are predominately nonresidential in composition. Nevertheless, the sample included neighborhoods within the higher SUHI zones adjacent to the central commercial district and to native-vegetation parklands, both of which tend to have high LST (Fig. 2). Second, census block data were employed because of our focus on the land architecture–LST relationship, which is more accurately captured at the fine-spatial grain of the census block rather than at the more coarse-spatial grain of the census block group. In a few cases, our sampled census blocks had 10 or fewer households, and household income data provided by the census are derived at the census block group level and applied to block level for our entire sample. These two issues may affect our results.

2.2.2. Land-cover classification

To examine the heterogeneous land architecture of neighborhoods requires detailed land-cover data. These data were derived through the image classification of the National Agricultural Imagery Program (NAIP) data, 1 m orthorized aerial photography taken from June 8–10, 2010. The NAIP dataset includes four spectral bands (red, green, blue, and near infrared band) with their radiances converted to a Digital Number ranging from 0–255, mosaicked at the county scale. The dataset was cookie-cut to the extent of the Central Arizona-Phoenix Long-term Ecological Research program (www.caplter.asu.edu), which covers most of the metro-Phoenix area, and preprocessed with pixel-based spectral transformations, which included *red*, *green*, and *blue* to *intensity*, *hue*, and *saturation*, *principal components analysis*, and Normalized Difference Vegetation Index (NDVI). An Object-Based Image Analysis (OBIA) was utilized to produce the land-cover classification (Li et al.,

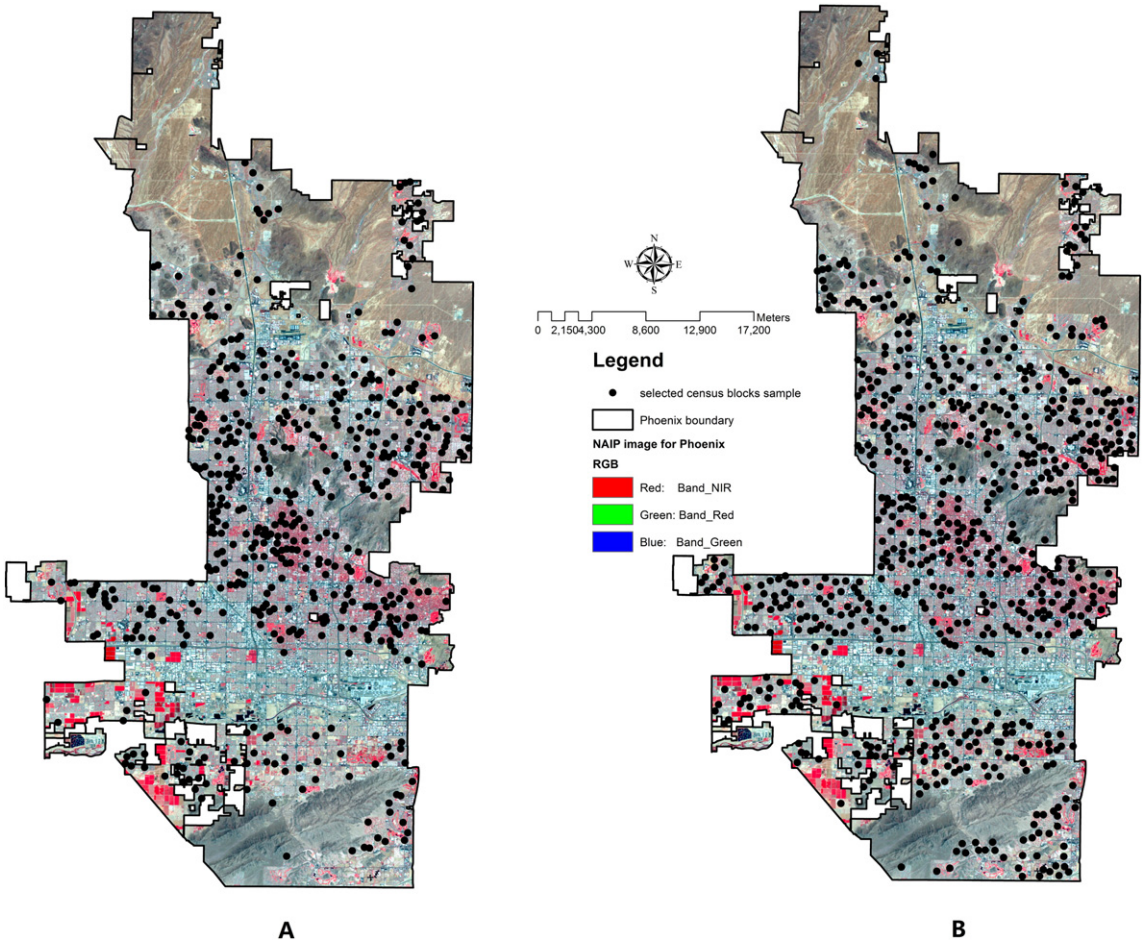

Fig. 1. The study area, random sample A and B census blocks, and NAIP-based land cover. The points indicate the selected census blocks, and the polygon is the boundary of the city of Phoenix. The background image is the NAIP data with near-infrared band, red band, and green band displayed on the red, green, and blue channel respectively.

2014b). This approach was built on a hierarchical image object network, with image segmentation algorithms (multi-resolution segmentation, multi-threshold segmentation, chessboard segmentation, and Quadtree segmentation) to divide the image into different levels of image objects. Image objects that belong to specific land-cover types maintain unique characteristics in terms of spectral, spatial, contextual, and geometric information. In addition, cadastral data in a GIS vector layer were used to regulate the boundary of each parcel. Expert knowledge decision rules were created based on those characteristics to delineate the land-cover types. All parcels and adjacent streets were analyzed for the selected neighborhoods. The land-cover mapping includes 12 classes with a 91.86% overall accuracy (Li et al., 2014b). Five classes (building, impervious surfaces, open soil, vegetation, and swimming pool) dominated our neighborhoods and were used in this analysis. The category "impervious surfaces" refers to roads, parking lots, and related features, but not to buildings.

Table 1
Description of the random sample selection for sample A and sample B.

		Sample A	Sample B
1	Number of initial randomly selected parcels	1000	1000
2	Number of parcels reduced by distance filter (1000 m)	723	787
3	Number of census blocks with parcels in #2 with distance filter (500 m)	523	545
4	Percent of selected census blocks for Phoenix	55%	57%
5	Number of parcels in selected census blocks	27,470	27,528
6	Number of residential parcels in selected census blocks	26,614	26,326
7	Percent of residential parcels in selected census blocks	97%	96%
8	Number of single family residential parcels (subset of #6)	21,505	24,167
9	Percent of single family residential parcels of total residential parcels (#6)	81%	92%
10	Number of multi-family residential parcels (subset of #6)	5109	2159
11	Percent of multi-family residential parcels of total residential parcels (#6)	19%	8%
12	Percent of residential parcels in selected census blocks	97%	96%
13	Number of non-residential parcels in selected census blocks	856	1202
14	Percent of non-residential parcels in selected census blocks	3%	4%

2.2.3. Land surface temperature

Landsat Thematic Mapper was used to derive LST: cloud free TM sensor (row = 37, path = 37) taken about 10 AM, on June 10, 2010. This date matched the three-day window in which the NAIP data (above) were derived. In addition, weather station data for that window (June 8–10), revealed highly similar temperatures and conditions, clear and calm, typical mid-morning weather for Phoenix in early June. The Landsat Band 6 thermal data (120 m) were re-projected to the Universal Transverse Mercator projection system Zone 12 N and converted to 30 m.

To estimate the LST from the Landsat TM thermal infrared band data, the Digital Numbers of sensors were converted to meaningful radiance using a spectral radiance scaling method (Eq. 1) (Chander & Groeneveld, 2009):

$$L_\lambda = \frac{LMAX_\lambda - LMIN_\lambda}{Q_{calmax} - Q_{calmin}} \times (Q_{cal} - Q_{calmin}) + LMIN_\lambda \quad (1)$$

where the L_λ is the cell value as radiance (W/(m^2 sr μm)), Q_{cal} is the quantized calibrated digital number, Q_{calmin} is the minimum quantized

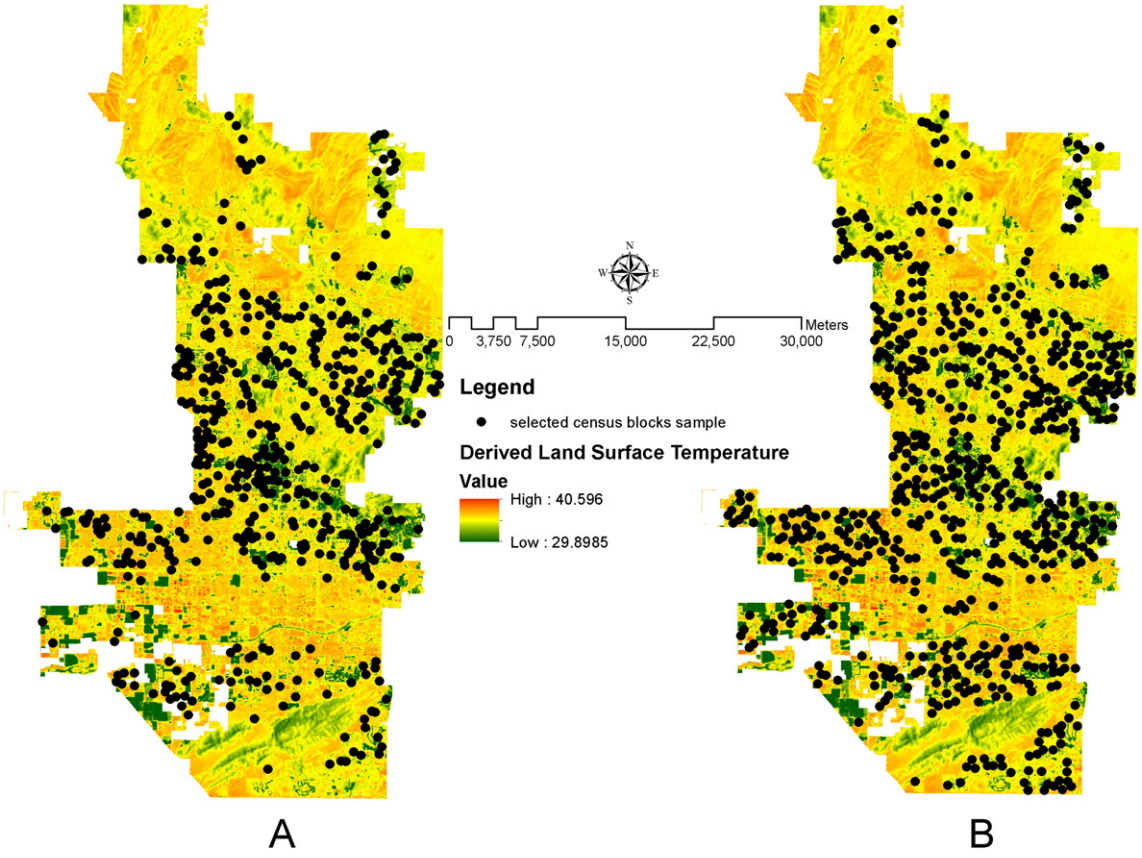

Fig. 2. Derived land surface temperatures for the city of Phoenix using Landsat TM and selected census blocks in samples A and B. The points represent the selected census blocks.

calibrated pixel value, and Q_{calmax} is the maximum quantized calibrated pixel value; $LMIN_\lambda$ is the spectral radiance scales to Q_{calmin}, $LMAX_\lambda$ is the spectral radiance scales to Q_{calmax}.

Spectral radiance was converted to brightness temperature by assuming the earth's surface is a black body (Eq. 2) (Chander, Markham, & Helder, 2009; Coll, Galve, Sánchez, & Caselles, 2010):

$$T_b = \frac{K_2}{\ln\left(\frac{K_1}{L_\lambda}+1\right)} \tag{2}$$

where T_b is the brightness temperature in Kelvin, L_λ is the cell value as radiance, K_1 (607.76 W / (m^2 sr μm)) and K_2 (1260.56 K) are the constants of Landsat TM calibration.

The brightness temperature was converted to kinetic temperature, or land surface temperature (Eq. 3) (Artis & Carnahan, 1982; Dakin, Pratt, Bibby, & Ross, 1985):

$$T_s = \frac{\mathrm{T}_b}{1+\left(\lambda \times \frac{T_b}{\rho}\right) ln\varepsilon} \tag{3}$$

where λ (11.5 μm) is the emitted radiance wavelength (Markham & Barker, 1985), the coefficient ρ (0.01438 mK) is generated from the equitation $\rho = hc/b$, in which h (6.626×10^{-34} Js) is the Planck's constant, c (2.998×10^8 m/s) is the velocity of light, and b (1.38×10^{-23} J/K) is the Boltzmann constant, and ε is the surface emissivity.

The estimation of land surface emissivity is one of the essential parameters to retrieve LST. Several methods can be used to calculate land surface emissivity (Gillespie, Matsunaga, & Rokugawa, 1998; Snyder, Wan, Zhang, & Feng, 1998). Our study utilized the simplified Normalized Difference Vegetation Index (NDVI) thresholds method ($NDVI^{THM}$) to obtain the values from Landsat imagery (Sobrino, Jimenez-Munoz, & Paolini, 2004; Sobrino et al., 2008). NDVI is calculated from the Landsat imagery with the following equation (Eq. 4):

$$NDVI = \frac{Band\ 4 – Band3}{Band\ 4 + Band3}. \tag{4}$$

Different approaches have been utilized to calculate the LST from the NDVI value. Like most urban areas, Phoenix is composed of heterogeneous and fragmented landscapes, requiring methods that account for emissivity in these conditions (e.g., Liu & Zhang, 2011). We adopted that of Sobrino et al. (2008) (Eq. 5):

$$\varepsilon = \varepsilon_v P_v + \varepsilon_s(1-P_v) + d\varepsilon. \tag{5}$$

Eq. 5 is the simplified version of the land surface emissivity calculation, where ε_v is the vegetation emissivity and ε_s is the emissivity for urban soil surface; P_v is the proportion of vegetation derived from an NDVI based empirical model (Eq. 7) by Carlson and Ripley (1997) and Sobrino et al. (2004, 2008); $d\varepsilon$ is the error in the model shown in Eq. 5, including the land surface geometrical distribution effect and internal reflections (Sobrino et al., 2004; Sobrino et al., 2008). The estimation of $d\varepsilon$ is given by (Eq. 6):

$$d\varepsilon = (1-\varepsilon_s)(1-P_v)F\varepsilon_v \tag{6}$$

where F (0.55) is a shape factor (Sobrino, Caselles, & Becker, 1990; Sobrino et al., 2004). In order to obtain more accurate and consistence values of P_v, we assign it 0.99 when $NDVI > NDVI_v$ and 0 when $NDVI < NDVI_s$ (where $_v$ and $_s$ refer to vegetation and soil). The $NDVI^{THM}$

methods described here estimate the surface emissivity for bare soil pixels (NDVI < $NDVI_s$) using the reflectivity value of red band ρred (Landsat TM band 3), and the equations are expressed as (Eqs. 7 & 8):

$$\varepsilon = \begin{cases} a + b\ \rho red \text{ when } NDVI < NDVIs \\ \varepsilon_v P_v + \varepsilon_s(1-P_v) + d\varepsilon \text{ when } NDVIs \le NDVI \le NDVIv \\ \varepsilon_v + d\varepsilon \text{ when } NDVI > NDVIv \end{cases} \quad (7)$$

$$P_v = \left[\frac{NDVI - NDVI_{min}}{NDVI_{max} - NDVI_{min}}\right]^2. \quad (8)$$

Adapting the approximation of vegetation and urban soil surface emissivity values from Sobrino et al. (2008), land surface emissivity is expressed as (Eq. 9):

$$\varepsilon = \begin{cases} 0.979 - 0.035\ \rho red \text{ when } NDVI < 0.2 \\ 0.986 + 0.004\ P_v \text{ when } 0.2 \le NDVI \le 0.5 \\ 0.99 \text{ when } NDVI > 0.5. \end{cases} \quad (9)$$

The derived LST (Fig. 2) describes the surface thermal condition for the city of Phoenix. Pixel values range from 29.9 °C to 40.6 °C, and the mean LST is 33.5 °C. Only a 0.1^0 C difference in LST separates the mean temperature for Sample A = 33.4 and Sample B = 33.5. Finally, the LSTs reported for each census block includes all parcels and streets within that block.

It is noteworthy that retrieving representative in-situ measurements to validate LST data from satellite images in heterogeneous environments is challenging. LST varies significantly over space and time, even at sub-grid resolution (Li et al., 2013). Vanos et al. (in press) found surface temperature differences of up to 30 °C between shaded and non-shaded surfaces on a playground in Phoenix at the touch scale (1 cm). These differences were not captured by an infrared MASTER super spectral image (6.8 m resolution) available to them. Due to a lack of high-resolution data, we can only qualitatively assess the accuracy of the LST product derived from Landsat TM.

The overall accuracy of LST from satellite-based thermal infrared (TIR) data depends on atmospheric and emissivity corrections. Jiménez-Muñoz and Sobrino (2006) assessed errors associated with LST estimation from TIR data and found that atmospheric effects typically lead to an error of 0.2 K to 0.7 K. Uncertainties in emissivity retrieval result in an error of 0.2 K to 0.4 K. The total minimum error to be expected without in-situ measurements is 0.8 K. Various other studies are in line with this accuracy assessment. Yu, Guo, and Wu (2014) retrieved LST from Landsat 8 TIRS and found that a radiative transfer equation-based method produced results with RMSE <1.0 K. Rozenstein, Qin, Derimian, and Karnieli (2014) used a split window algorithm to estimate LST from Landsat 8 at RMSE = 0.93 K. We expect the accuracy of our LST calculation to be comparable to those results.

2.2.4. Land-architecture data

Neighborhood-scale (entire census block) land architecture measures were derived from the land-cover (2.2.3) and census block data. Measures include the area and compactness pattern index of each land-cover type, and the same index of the census block (Table 2). The area of each land-cover type (area_class#) was determined by the number of pixels of each type within the census block unit. The spatial pattern indicator of the land-cover types was calculated using a new compactness pattern measure, the Normalized Moment of Inertia (NMI) (Li et al., 2013a). As described below, NMI has been demonstrated to be more effective and accurate than other measures of the compactness of a patch (land-cover unit) and the concentration of patches (Miller, 1953; Schwartzberg, 1965; McGarigal & Marks, 1995; Li et al., 2014a). Compactness measures the extent to which the shape is spread out from its center; a circle constitutes the most compact shape. Concentration measures the compactness of multiple patches, a product of the distances among patches and the compactness/moment of each single patch.

The NMI measure draws on the second moment of inertia (aka, area moment of inertia) to measure the degree to which all elements on a natural planar shape *i* are concentrated. Mathematically, the second moment of a shape $I_i^{G_i}$ about an axis perpendicular to it and passing through its centroid G_i can be computed from:

$$I_i^{G_i} = \int d^2 da_i \quad (10)$$

where
da_i is the infinitely small area on the shape *i*, *d* is the distance from da_i to G_i. The normalized value NMI, can then be derived by comparing $I_i^{G_i}$ to the second moment of a circle I_0 which has the same area of the shape:

$$NMI = \frac{I_0}{I_i^{G_i}}. \quad (11)$$

Given that the area moment of a circle with area *A* is known as $\frac{A^2}{2\pi}$, NMI can then be represented as:

$$NMI = \frac{A^2}{2\pi I_i^{G_i}}. \quad (12)$$

The NMI has a range of 0, 1, with 0 representing an infinitely elongated shape, and 1 representing the most compact shape, a circle.

Several prominent features of NMI make it suitable for identifying the spatial configuration pattern of land architecture. First, NMI is scale-independent: patches with the same shape but different size will be given the same value, providing a more consistent view of the land configuration than a PARA (perimeter-area ratio) approach, as in FRAGSTATS (McGarigal, Cushman, & Ene, 2012). Second, different from other FRAGSTATS shape indices, such as the fractal dimension index, the linearity index, and the related circumscribing circle index, which focus more on measuring the edge complexity by considering perimeter as an important factor, the NMI pays more attention to the shape itself rather than the roughness of the edge boundary. Moreover, the NMI is not only capable of measuring shape compactness of a single object, but it can also quantify the overall compactness pattern for target objects as a whole. Therefore, it has the ability to evaluate accurately how patches/sub-patches are concentrated or dispersed within an area. This is an important consideration for neighborhood study, in which the basic area, a neighborhood, always contains more than one object of a given land type (e.g., buildings) dispersed at different locations within the neighborhood.

Fig. 3 demonstrates the computation of NMI for multi-objects. Supposing there are three objects within the study area, each has area moment I_1, I_2, and I_3, and areas of A_1, A_2, and A_3, the area moment I_{entire} of the three objects composited together can be represented as:

$$I_{entire} = \sum_{i=1}^{n} I_i + \sum_{i=1}^{n} A_i d_i^2 \quad (13)$$

where $n = 3$ in this case, d_i is the distance from shape *i*'s centroid to the centroid (X,Y) of the new object. If (x_i, y_i) is the coordinates of the centroid for shape *i*, then (X, Y) can be computed as:

$$X = \frac{\sum_{i=1}^{n} A_i x_i}{n},\ Y = \frac{\sum_{i=1}^{n} A_i y_i}{n}. \quad (14)$$

Table 2
Land architecture metrics and their descriptive statistics. Sample A and B on top and bottom of each row-column numeric entry, respectively.

Factor abbreviation	Factor description	Range	Mean	Std. deviation	Std. error mean
Land architecture					
Land composition					
area1	Area building cover (m^2)	458.42–16,752.41	1245.84	887.00	38.78
		319.43–13,859.25	902.00	660.52	28.19
area2	Area impervious surfaces(m^2)	361.18–29,100.47	4935.30	4855.49	212.31
		480.67–22,051.06	3090.00	2965.75	126.57
area3	Area soil cover (m^2)	119.17–53,963.01	7715.21	7298.62	319.14
		940.31–21,272.91	5215.50	4157.45	177.43
area4	Area vegetation cover (m^2)	138.38–25,034.44	3760.95	3938.98	172.24
		171.30–26,995.83	2695.50	3483.21	148.66
area5	Area swimming pool cover (m^2)	0.00–224.79	125.66	38.50	1.68
		0.00–274.32	92.37	72.47	4.26
Land configuration					
nmi1	Compactness pattern index building cover	0.01–0.84	0.17	0.00	0.00
		0.02–0.42	0.17	0.07	0.00
nmi2	Compactness pattern index road	0.01–0.54	0.13	0.09	0.00
		0.01–0.53	0.11	0.06	0.00
nmi3	Compactness pattern index soil cover	0.02–0.90	0.26	0.13	0.01
		0.03–0.73	0.27	0.12	0.00
nmi4	Compactness pattern index vegetation cover	0.01–0.66	0.13	0.10	0.00
		0.01–0.59	0.13	0.09	0.00
nmi5	Compactness pattern index swimming pool cover	0.00–0.85	0.02	0.08	0.00
		0.00–0.98	0.11	0.27	0.01
nmi_block	Compactness pattern index census block	0.02–1.00	0.66	0.19	0.01
		0.01–0.09	0.71	0.20	0.01
Cadastral–demographic–economic variables (CDE)					
Households	Total number of households per census block	182–1378	569.27	171.56	7.50
		220–1378	568.84	190.52	8.13
median_hh	Median of household income in $ of census blocks	17,500–148,958	64,086.84	28,492.56	1245.89
		22,393–170,179	65,229.23	30,681.10	1309.44
pop_den	Total population density (per m^2)of census blocks	0.01–0.42	0.23	0.16	0.00
		0.01–0.41	0.13	0.05	0.00
hispnic_den	Hispanic population (of any race) density (per m^2) of census blocks	0.00–0.87	0.28	0.12	0.00
		0.00–0.37	0.31	0.02	0.00
white_den	White population density (per m^2) of census blocks	0.00–0.66	0.11	0.08	0.00
		0.00–0.39	0.12	0.08	0.00
afam_den	African American population density (per m^2) of census blocks	0.00–0.02	0.01	0.02	0.00
		0.00–0.22	0.01	0.01	0.00
amind_den	American Indian population density (per m^2) of census blocks	0.00–0.02	0.00	0.01	0.00
		0.00–0.01	0.00	0.01	0.00
asian_den	Asian population density (per m^2) of census blocks	0.00–0.11	0.01	0.01	0.00
		0.00–0.14	0.01	0.01	0.00
total_area_block	Total area (m^2) of census blocks	688–19,865	6692.27	4782.32	209.34
		918–23,315	4483.24	3474.23	148.02
total_edge_length	Total edge length (m) of census blocks	172.76–5535.11	1339.26	837.11	36.60
		100.58–8394.19	501.74	658.98	24.29
ave_area	Average area (m^2) of parcels of census blocks	758–5369	1911.38	747.90	32.70
		439–6750	1057.19	863.87	36.87

According to Eq.11, the NMI of the composited object can then become:

$$NMI = \frac{I_{0\_entire}}{I_{entire}} = \frac{\left(\sum_{i=1}^{n} A_i\right)^2}{2\pi\left(\sum_{i=1}^{n} I_i + \sum_{i=1}^{n} A_i d_i^2\right)}. \quad (15)$$

Benefitting from this additive nature, the compactness index of a composited object can be easily obtained. In a land-use classification map, the pixels with the same type/value will be collectively summed up (non-linearly) to compute the overall compactness. With this indicator, both the shape of a single object and the concentration of multiple objects in a neighborhood can be detected. Using the above approach, we calculated the area moment and the compactness pattern value for each land-use type (e.g., building, soil) and the compactness of the neighborhood boundary itself with the objective to study how well the composition of these objects impacts the local surface temperature.

2.2.5. Cadastral–demographic–economic data

Cadastral–demographic–economic (CDE) variables were collected or calculated from the City of Phoenix cadastral data, the 2010 U.S. Census, and our land-cover classification. These variables included the following for each census block: the median household income, number of parcels and average parcel sizes, population density (total population/area), population densities of residents by ethnicity (i.e., Hispanic of any race and non-Hispanic White, African-American, American Indian-Alaskan Native, Asian, Native Hawaiian and other Pacific Islanders, and others), the total area of each neighborhood/census block, and the total edge length of the census block (Table 2).

2.3. Statistical analysis

We joined all data spatially, including land architecture measures, CDE variables, and the aggregated LST (average per census block) derived from the Landsat image with the point shape file of the spatial distribution of the sampled census blocks. Multiple ordinary least squares regressions (OLS) were used to determine the effects of land

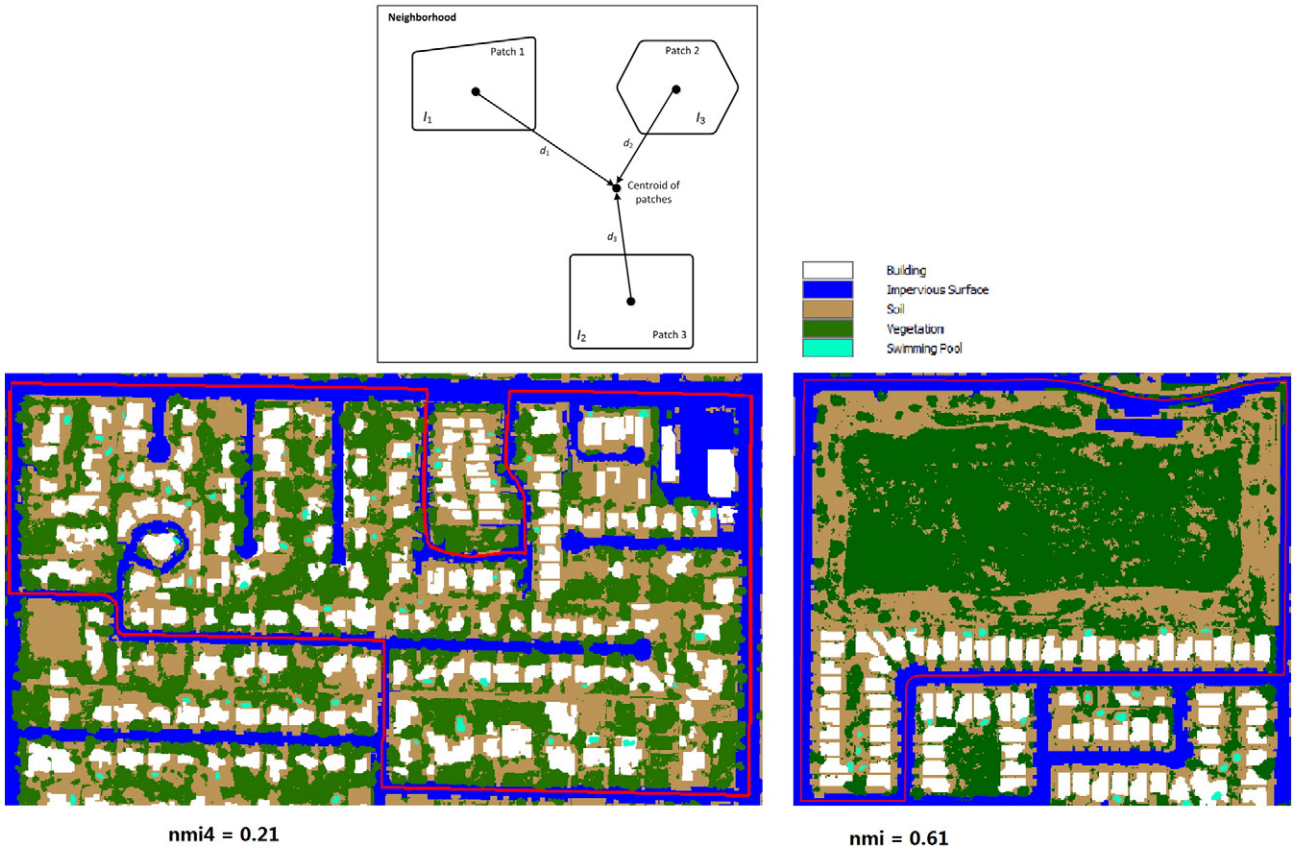

Fig. 3. An example of multi-patch object and parameters (d = distance and I = moment of inertia) used to compute compactness of multiple patches in one neighborhood (see text). The images show two neighborhoods with approximately the same area of vegetation but contrasting NMI values: the image on the left has a low NMI value (0.21) for vegetation and the image on the right has a high NMI value (0.61) for vegetation.

architecture and demographic-economic variables (independent variables) on the LST (dependent variable). In order to process a valid OLS and avoid type I errors that happen when the error terms of the OLS are not independent (De Knegt et al., 2010; Li et al., 2012; Lichstein, Simons, Shriner, & Franzreb, 2002), we further tested each variable for spatial auto-correlation using global Moran's I. Each variable has a Moran's I ≤ 0.1, and is not significant at the 0.1 level, indicating the weak spatial autocorrelation within the independent variables and thus, greater confidence in the validity of OLS parameter estimates. Table 2 presents descriptive statistics on the independent variables used in the regression models.

Initially joined in the regression, the following variables were removed because they were not statistically significant with LST or were collinear with other variables in the models listed in Table 3: NMI per census block, average parcel size, total edge of houses, total edge length of census block, and shape index of the residential neighborhood, total area of the neighborhoods/census block, compactness pattern index (NMI) of the census block, total number of households in the census block, and American Indian, Asian, African American, Hispanic and White population density.

We explored the hypotheses through four scenarios involving seven models (all the initial independent variables in each model are listed in Table 2): (1) LST — land composition model; (2) LST — land configuration model; (3) LST — CDE factors model; (4) LST — land composition + land configuration; (5) LST — land composition + CDE factors model; (6) LST — land configuration model + CDE factors model; and (7) LST — land architecture (composition and configuration) + CDE factors model. We conducted the forward stepwise selection with the least Akaike information criterion with a correction and significance level at $\alpha = 0.01$ to create the OLS models for each scenario. The selection of the explanatory variables also involved the examination of the variance inflation factor, a factor to test the multicollinearity among the explanatory variables. All the models have variance inflation factor values less than two for the explanatory variables. Finally, an incremental R^2 test was employed to determine the explained variance gained by adding variables to the base OLS models.

Table 3
Correlation coefficients of seven models for samples A and B ($p < 0.01$).

	Model	Sample A R^2	Sample A adjust R^2	Sample B R^2	Sample B adjust R^2
1	Land composition	0.15	0.14	0.17	0.16
2	Land configuration	0.52	0.51	0.54	0.54
3	Cadastral–demographic–economic variables (CDE)	0.21	0.21	0.15	0.15
4	Composition + configuration	0.54	0.54	0.57	0.56
5	Composition + CDE	0.31	0.31	0.27	0.27
6	Configuration + CDE	0.64	0.63	0.63	0.63
7	Composition + configuration + CDE	0.65	0.64	0.64	0.64

3. Results

The seven OLS models are statistically significant ($p < 0.001$) as are 19 of the 24 added variables in the incremental R^2 test (Tables 3 & 4). The correlation results by model are very close for both samples in the OLS and incremental R^2 test. Significantly, land configuration as a lone variable or with CDE variables provides stronger associations with mean neighborhood LST than does land composition in both samples of the OLS models. This observation is further supported by the extremely small (0.01) improvement of Model 7 (composition + configuration + CDE)

Table 4
Incremental R^2 test: the added R^2 value to the base models of the models with additional independent variables.

Models with addition of independent variables									
		Composition + configuration		Composition + CDE		Configuration + CDE		Composition + configuration + CDE	
		Sample A	Sample B	Sample A	Sample B	Sample A	Sample B	Sample A	Sample B
Base models	Land composition	0.269[a]	0.269[a]	0.012	0.202[a]			0.521[a]	0.445[a]
	Land configuration	0.015	0.029[a]			0.257[a]	0.185[a]	0.261[a]	0.203[a]
	Cadastral–demographic–economic factors (CDE)			0.127[a]	0.093[a]	0.388[a]	0.316[a]	0.635[a]	0.334[a]
	Composition + configuration							0.232[a]	0.162[a]
	Composition + CDE							0.514[a]	0.242[a]
	Configuration + CDE							0.004	0.018[a]

[a] Denotes increments significant at $\alpha = 0.001$ level (F test).

over Model 6 (configuration + CDE) (Table 3). It is additionally supported by the small correlation increments that land configuration gains by adding other variables and the much larger increments gained by those variables when added to land configuration (Table 4). Equally significant, strong correlations, $R^2 = 0.54$ to 0.65, were generated for various combinations of land architecture and CDE variables (Table 3).

The significant variables in all models for both samples display the same impact (positive or negative) on LST (Table 5). Similar to the results of Jenerette et al. (2007, 2011), vegetation and swimming pools decrease LST, whereas buildings, soil, and impervious surfaces increase it. Importantly to our case, increases in the compactness and concentration of bare soil increase LST, while those characteristics for vegetation decrease it. In addition, a positive association exists between population density and LST, whereas an inverse relationship exists between median household income (Census data designation) of neighborhoods and LST.

4. Discussions

Although the relationships between LST and vegetation and CDE factors have been studied previously (Hanamean et al., 2003; Saunders, Chen, Crow, & Brosofske, 1998, Smith and Smith & Johnson, 2004; Jenerette et al., 2007; Martin, 2008; Jenerette et al., 2011; Myint, Wentz, Brazel, & Quattrochi, 2013), examination of the kind undertaken in this study has been restricted owing to the paucity of use of high-

Table 5
Impact of independent and/or joint land architecture and cadastral–demographic–economic factors on LST. Descriptions of the independent variables can be found in Table 2.

	Sample A			Sample B		
Model	Variables	Coefficient	Std. coefficient	Variables	Coefficient	Std. coefficient
1	area3	0.0079	0.3099	area3	0.0026	0.4307
	area4	−0.0036	−0.5381	area4	−0.0018	−0.5462
				area5	−0.0001	−0.1478
2	NMI1	129.2561	0.2402	NMI1	75.0498	0.1543
	NMI3	45.4130	0.1428	NMI3	48.3265	0.1741
	NMI4	−270.3970	−0.6606	NMI4	−248.4714	−0.6778
				NMI5	16.4240	0.1122
3	total_den	13,780.3044	0.4592	median_hh	−0.0004	−0.3826
4	area5	−0.0027	−0.1724	area1	−0.0032	−0.2235
	NMI1	112.5680	0.2092	area2	0.0021	0.1732
	NMI3	48.6427	0.1530	area5	−0.0010	−0.1211
	NMI4	−258.5293	−0.6316	NMI1	66.5219	0.1368
				NMI3	48.4170	0.1744
				NMI4	−246.3083	−0.6719
				NMI5	15.1407	0.1034
5	area3	0.0010	0.3947	area3	0.0025	0.4155
	area4	−0.0030	−0.4460	area4	−0.0016	−0.4860
	total_den	13,189.1067	0.4396	area5	−0.0010	−0.1261
				median_hh	−0.0004	−0.3342
6	NMI1	99.4659	0.1849	NMI1	59.2853	0.1219
	NMI3	64.1074	0.2016	NMI3	59.6380	0.2148
	NMI4	−252.1356	−0.6160	NMI4	−236.7961	−0.6460
	median_hh	−0.0004	−0.3601	median_hh	−0.0004	−0.3323
7	area5	−0.0002	−0.0982	area5	−0.0009	−0.1058
	NMI1	91.7325	0.1705	NMI1	52.6507	0.1082
	NMI3	64.8338	0.2039	NMI3	59.3241	0.2137
	NMI4	−246.4618	−0.6022	NMI4	−233.5761	−0.6372
	median_hh	−0.0004	−0.3387	median_hh	−0.0004	−0.3244

The following independent variables were removed owing to multicollinearity:
- Total area of the census block
- Compactness pattern index (NMI) of the census block
- Total edge length of the census block
- Asian population density
- American Indian population density
- African American population density
- Hispanic population density
- Total population density of the census block
- Total number of households in the neighborhood

All independent variables in this table are significant at $\alpha = 0.001$ level. The dependent variable is the mean neighborhood (census block) LST. The R^2 of each model is in Table 3.
Area and NMI #s refer to
1: building
2: impervious surfaces
3: soil
4: vegetation
5: swimming pool

resolution land-cover data and effective shape/configuration measures of individual land covers (but see Zheng et al., 2014). Our results provide insights into testable hypotheses about land architecture, point to characteristics of that architecture that may serve to reduce the SUHI effect during the summer day, and offer insights to studies of neighborhood inequalities with respect to SUHI intensity.

4.1. The implications of land architecture on LST

Hypothesis 1. *that land architecture affects summer daytime LST, is supported.* Land composition and configuration (or land architecture; Model 4, Table 3) of the sample neighborhoods in Phoenix considerably exceeded CDE variables (Model 3, Table 3) in terms of impacts on LST. The role of configuration is elaborated below (4.2). Here we focus on composition.

Table 5 lists the role of the independent variables on daytime LST at the neighborhood level. Consistent results across the models include: increasing area of vegetation and swimming pools lowers LST, owing to evapotranspiration, whereas increasing area of bare soils has the opposite effect, owing to rapid reradiation of solar energy, especially in this hot, arid environment (Table 5). These results are consistent with those found elsewhere (Martin, 2008, Akbari 2009, Li et al., 2011; Weng & Fu, 2014) and in recent studies of the Phoenix area (Jenerette et al., 2007; Jenerette et al., 2011; Jenerette et al., 2015; Myint et al., 2013). Buildings also reradiate heat, but the area of them proved significant only in Sample B of Model 4, surprisingly with a negative LST relationship. Further research is required to determine why the two samples differed and the cause of the negative relationship, the latter perhaps influenced by differences in the albedo of the predominant roof-tops in different neighborhoods. Surprisingly, the area of impervious surfaces is significant only in the same sample and model as building, but increases LST as expected. The absence of this variable in our other models requires further investigation, given its prominence in other studies (e.g., Zheng et al., 2014).

Hypothesis 2. *that land composition affects summer daytime LST more strongly than land configuration, is not supported.* This hypothesis is implied in the various works that have found a strong and significant relationship between the area or area fraction of specific types of land covers and LST. It is directly supported by at least one study that considered both land composition and configuration in the Baltimore area (Zhou et al., 2011). In our models, however, land configuration has a much stronger correlation with LST than does land composition as noted above (Tables 3 & 4), although its positive or negative impact on LST depends on the land-cover classes in question (Table 5). This distinction between configuration and composition remains when CDE factors are added (Models 5 & 6; Table 3). It is noteworthy that our measure of compactness and concentration (NMI) of building, soil, and vegetation appear in all models, complete with the expected LST relationships (building and soil increasing LST and vegetation cooling). The uniformity in compactness and concentration of swimming pools likely explains the omission of this land-cover class. As noted for composition, the absence of impervious surfaces in the results requires investigation, perhaps reflecting the uniformity among road networks in residential neighborhoods. Finally, consistent with work by Zhou et al. (2011), joining land composition and configuration (land architecture) improves the correlation with LST, but only marginally (Model 4, Table 3).

4.2. The influence of cadastral–demographic–economic factors (CDE)

Hypothesis 3. *that land architecture has a stronger relation to summer daytime LST than do CDE factors, is supported.* Land cover is the proximate source of LST, and similar architectures should produce similar LSTs, all else held constant. In contrast, CDE variables are more distal to LST because the characteristics of households and neighborhoods are associated with land covers (and land uses) and operate only indirectly on LST through land cover (Jenerette et al., 2007). For these reasons, land architecture is expected to be more strongly associated with LST. Similar architectures, however, may be related to economic wealth and the ability to pay for the installation and maintenance of landscaping (e.g., Harlan et al., 2009) as well as to perceptions of desirable yard-scapes, age of neighborhood, rules of HOAs, or other such factors (e.g., Larson, Casagrande, Harlan, & Yabiku, 2009a). In our models, CDE variables account for a much smaller amount of the explained variance (Model 3) in LST than does land architecture (Model 4) in both samples, as well as not adding significant R^2 increments to composition and configuration (Table 4).

The only significant CDE variables are population density and median household income, which increase and decrease LST, respectively. These results are consistent with findings from other research on Phoenix (Buyantuyev & Wu, 2010; Harlan et al., 2006; Huang et al., 2011; Jenerette et al., 2007; Martin, 2008) indicating lower levels of income and vegetation and higher levels of occupation density concentrated toward the center of the metro-Phoenix SUHI, and increasing levels of incomes either at distance from this center or associated with the use of turf grass (Connors et al., 2013). All other CDE variables were removed from the analysis because they were collinear with other independent variables.

Beyond the hypotheses it is noteworthy that the trends in the model outcomes for both samples are consistent as are the correlation coefficients, with the exception of slightly lower correlations for Sample B in Models 3 and 5 (Table 3), suggesting modest differences in CDE variables in the samples. This distinction signals the need for future exploration of the role of income, preferences, and HOA rules on land covers. In older parts of Phoenix, higher income neighborhoods tend to maintain more vegetation, including turf grass, than lower-income areas (Jenerette et al., 2007, 2011; Larson et al., 2009a). Newer high-end neighborhoods, however, commonly require at least some desert- or xeric-scaping (see Chow & Brazel, 2012), which, through the use of the NMI assessment, renders composition characteristics similar to those displayed in lower income (largely Hispanic) neighborhoods with large amounts of bare soil, possibly resulting in similar LSTs. On-the-ground observation of higher income, desert-scaped and lower income, Hispanic dominated parcels, however, indicates substantial differences in landscaping.

It is also noteworthy that the results reported here using the more recent Sobrino et al. (2008) approach are significantly improved relative to those generated from their former approach (Sobrino et al., 2004). The subdivision of the NDVIs and NDVIv and the use of the red band provides a more accurate assessment of LST in the heterogeneous urban environment, especially in regard to our bare soil class observed during the morning.

Overall, our findings are consistent with the emerging literature signaling that UHI effects are affected by the land-cover composition of the urban area (e.g.Georgescu et al., 2011; Zheng et al., 2014; Zhou et al., 2014), but differs from most of this research by demonstrating the strong role of land configuration as well. The implications of corpus of these works is that urban areas, especially those in warm desert climates, could ameliorate the SUHI effect and the UHI effect at large by attention to the design of neighborhoods and, perhaps, parcels of new developments and to the reshaping of existing neighborhoods. The essential elements of this design focus on increasing the compactness and concentration of vegetation covers and decreasing the same for buildings and impervious surfaces. Much more work is required, however, to provide metrics and elaboration (e.g., shape) for such configurations.

5. Study limitations

This study is exploratory and the reported results should be interpreted in terms of the study's limitations. Foremost, the spatial resolutions of the LST (120 m) and land cover (1 m) are incongruent. As a consequence, the LST constitutes an average of multiple land covers applied to individual land-cover types. The smaller and less compact the individual land-cover, the more likely its "real" LST deviates from that applied here. In addition, we assume that the LST data generated from a single Landsat image is representative of typical June mid-morning conditions in Phoenix. Future research should examine other summer days and time, foremost late summer afternoons when maximum temperature is reached, especially affecting impervious surfaces and buildings, and other images of the metropolitan region. Similar examinations for different seasons are required, as are alternative means of establishing LSTs (e.g.Liu & Zhang, 2011; Mitraka et al., 2013; Sobrino et al., 2009), including "unmixing" techniques reported by Mitraka et al. (2013).

In addition, census blocks need not capture the neighborhood as defined by, for example, developers, HOAs, or other factors that may be used to capture some coherent character of residential parcels, especially in regard to parcel-level land architecture. Significantly, our neighborhood selection was generated by a random sample of single family residential parcels and did not control for any other parcel types, such as multiple residential, recreational, or commercial parcels within the identified residential area. The NMI measure of configuration employed in this study is not compared to results from the use of other shape measures, such as FRAGSTATS, to determine their compatibility or the influence of different metric sets on the outcomes. Additionally, the independent variables employed were selected by the research team, possibly leading to an omitted variable bias. We did explore backward correction steps in the regressions and found nothing significant. In the future, however, we will explore quantile regressions. Finally, our focus on linking as directly as possible land architecture and LST at the finest spatial grain as possible led us to the use of demographic and socioeconomic data at the U.S. Census block level, rather than the larger census block group. How this level assessment affected the model results will be examined in the future.

6. Conclusions

Employing fine-resolution (1 m) land-cover data and meso-resolution (120 m) LST data focused on U.S. Census blocks of Phoenix, AZ, demonstrates the important role of land architecture on the neighborhood SUHI effect. Recognizing its exploratory nature, this study is the first to indicate that land configuration is more important in its impacts on LST than land composition. That this finding reflects our use of a new configuration metric, the NMI, deserves research attention and comparison with other configuration metrics. Consistent with a set of recent studies, ours demonstrates that the compactness and concentration of vegetation has the largest cooling impact on LST at the neighborhood scale (census block).

Overall, our results suggest that land architecture of neighborhoods of Phoenix affect LST and the SUHI, and that this architecture is critical to neighborhood LST. This result suggests that care in the development or rearrangement in the composition and configuration of the land-cover of neighborhoods, including at the parcel level, can be used to ameliorate the UHI effect.

Acknowledgments

This project was supported by the National Science Foundation under Grant No. SES-0951366, NSF DMS Grant No. 1419593 and USDA NIFA Grant No. 2015-67003-23508; Decision Center for a Desert City II: Urban Climate Adaptation and Gant No. BCS-1026865, Central Arizona–Phoenix Long-Term Ecological Research (CAP LTER) and undertaken through the Environmental Remote Sensing and Geoinformatics Lab (ERSG) of the CAP-LTER, the Julie Ann Wrigley Global Institute of Sustainability, and School of Geographical Sciences and Urban Planning. The authors thank the reviewers of earlier versions of this paper for their insights and comments, as well as input from John Rogan and Arthur Elmes.

References

Akbari, H., Pomerantz, M., & Taha, H. (2001). Cool surfaces and shade trees to reduce energy use and improve air quality in urban areas. *Solar Energy*, *70*, 295–310.
Arnfield, A.J. (2003). Two decades of urban climate research: a review of turbulence, exchanges of energy and water, and the urban heat island. *International Journal of Climatology*, *23*, 1–26.
Artis, D.A., & Carnahan, W.H. (1982). Survey of emissivity variability in thermography of urban areas. *Remote Sensing of Environment*, *12*, 313–329.
Buyantuyev, A., & Wu, J. (2010). Urban heat islands and landscape heterogeneity: Linking spatiotemporal variations in surface temperatures to land-cover and socioeconomic patterns. *Landscape Ecology*, *25*, 17–33.
Carlson, T.N., & Ripley, D.A. (1997). On the relation between NDVI, fractional vegetation cover, and leaf area index. *Remote Sensing of Environment*, *62*, 241–252.
Chander, G., & Groeneveld, D.P. (2009). Intra-annual NDVI validation of the Landsat 5 TM radiometric calibration. *International Journal of Remote Sensing*, *30*, 1621–1628.
Chander, G., Markham, B.L., & Helder, D.L. (2009). Summary of current radiometric calibration coefficients for Landsat MSS, TM, ETM+, and EO-1 ALI sensors. *Remote Sensing of Environment*, *113*, 893–903.
Chen, X. -L., Zhao, H. -M., Li, P. -X., & Yin, Z. -Y. (2006). Remote sensing image-based analysis of the relationship between urban heat island and land use/cover changes. *Remote Sensing of Environment*, *104*, 133–146.
Chow, W.T.L., & Brazel, A.J. (2012). Assessing xeriscaping as a sustainable heat island mitigation approach for a desert city. *Building and Environment*, *47* (170–18).
Chow, W.T.L., Chuang, W., & Gober, P. (2012). Vulnerability to extreme heat in metropolitan phoenix: Spatial, temporal, and demographic dimensions. *The Professional Geographer*, *64*, 286–302.
Coll, C., Galve, J.M., Sánchez, J.M., & Caselles, V. (2010). Validation of landsat-7/ETM+ thermal-band calibration and atmospheric correction with ground-based measurements. *IEEE Transactions on Geoscience and Remote Sensing*, *48*, 547–555.
Connors, J.P., Galletti, C.S., & Chow, W.T. (2013). Landscape configuration and urban heat island effects: Assessing the relationship between landscape characteristics and land surface temperature in Phoenix, Arizona. *Landscape Ecology*, *28*, 271–283.
Dakin, J.P., Pratt, D.J., Bibby, G.W., & Ross, J.N. (1985). Distributed optical fiber Raman temperature sensor using a semiconductor light source and detectors. *Electronics Letters*, *21*, 569–570.
De Knegt, H., van Langevelde, F., Coughenour, M., Skidmore, A., de Boer, W., Heitkönig, I., ... Prins, H. (2010). Spatial autocorrelation and the scaling of species—environment relationships. *Ecology*, *91*, 2455–2465.
Georgescu, M., Moustaoui, M., Mahalov, A., & Dudhia, J. (2011). An alternative explanation of the semiarid urban area "oasis effect". *Journal of Geophysical Research*, *116*, D24113. http://dx.doi.org/10.1029/2011JD016720.
Gillespie, A.R., Matsunaga, T., & Rokugawa, S. (1998). Temperature and emissivity separation from advanced spaceborne thermal emission and reflection radiometer (ASTER) images. *IEEE Transactions on Geoscience and Remote Sensing*, *36*, 1113–1126.
Gober, P., Kirkwood, C.W., Balling, R.C., Jr., Ellis, A.W., & Deitrick, S. (2009). Water planning under climatic uncertainty in Phoenix: Why we need a new paradigm. *Annals of the Association of American Geographers*, *100*, 356–372.
Golany, G.S. (1996). Urban design morphology and thermal performance. *Atmospheric Environment*, *30*, 455–465.
Hanamean, J.R., Jr., Pielke, R.A., Sr., Castro, C.L., Ojima, D.S., Reed, B.C., & Gao, Z. (2003). Vegetation impacts on maximum and minimum temperatures in northeast Colorado. *Meteorological Applications*, *10*, 203–215.
Harlan, S.L., Brazel, A.J., Prashad, L., Stefanov, W.L., & Larsen, L. (2006). Neighborhood microclimates and vulnerability to heat stress. *Social Science & Medicine*, *63*, 2847–2863.
Harlan, S. L., Yabiku, S. T., Larsen, L., & Brazel, A. J. (2009). Household water consumption in an arid city: Affluence, affordance, and attitudes. *Society and Natural Resources*, *22*, 691–709. http://dx.doi.org/10.1080/08941920802064679.
Harlan, S.L., Declet-Barreto, J.H., Stefanov, W.L., & Petitti, D.B. (2013). Neighborhood effects on heat deaths: Social and environmental predictors of vulnerability in Maricopa County, Arizona. *Environmental Health Perspectives*, *121*, 197–204.
Hawkins, T.W., Brazel, A.J., Stefanov, W.L., Bigler, W., & Saffell, E.M. (2004). The role of rural variability in urban heat island determination for Phoenix, Arizona. *Journal of Applied Meteorology*, *43*, 476–486.
He, J.F., Liu, J.Y., Zhuang, D.F., Zhang, W., & Liu, M.L. (2007). Assessing the effect of land use/land cover change on the change of urban heat island intensity. *Theoretical and Applied Climatology*, *90*, 217–226.
Hondula, D.M., Davis, R.E., Leisten, M.J., Saha, M.V., Veazay, L.M., & Wegner, C.R. (2012). Fine-scale spatial variability of heat-related mortality in Philadelphia County, USA, from 1983–2008: A case-series analysis. *Environmental Health*, *11*, 1–11.
Hondula, D.M., Vanos, J.K., & Gosling, S.N. (2013). The SSC: A decade of climate–health research and future directions. *International Journal of Biometeorology*, *58*, 1–12.
Huang, G., Zhou, W., & Cadenasso, M.L. (2011). Is everyone hot in the city? Spatial pattern of land surface temperatures, land cover and neighborhood socioeconomic characteristics in Baltimore, MD. *Journal of Environmental Management*, *92*, 1753–1759.

Jenerette, G.D., Harlan, S.L., Brazel, A., Jones, N., Larsen, L., & Stefanov, W.L. (2007). Regional relationships between surface temperature, vegetation, and human settlement in a rapidly urbanizing ecosystem. *Landscape Ecology*, *22*, 353–365.

Jenerette, G.D., Harlan, S.L., Stefanov, W., Buyantuev, A., Stefanov, W.L., Declet-Barreto, J., ... Li, X. (2015). Micro-scale urban surface temperatures are related to land-cover features and residential heat related health impacts in phoenix, AZ USA. *Landscape Ecology*. http://dx.doi.org/10.1007/s10980-015-0284-3.

Jenerette, G.D., Harlan, S.L., Stefanov, W., & Martin, C. (2011). Ecosystem services and urban heat riskscape moderation: Water, green spaces, and social inequality in Phoenix, USA. *Ecological Applications*, *21*, 2637–2651.

Jiménez-Muñoz, J.C., & Sobrino, J.A. (2006). Error sources on the land surface temperature retrieved from thermal infrared single channel remote sensing data. *International Journal of Remote Sensing*, *27*, 999–1014.

Kalnay, E., & Cai, M. (2003). Impact of urbanization and land-use change on climate. *Nature*, *423*, 528–553.

Kane, K., Connors, J.P., & Galletti, C.S. (2014). Beyond fragmentation at the fringe: A path-dependent, high-resolution analysis of urban land cover in Phoenix, Arizona. *Applied Geography*, *52*, 123–134.

Larson, K.L., Casagrande, D., Harlan, S.L., & Yabiku, S.T. (2009a). Residents' yard choices and rationales in a desert city: Social priorities, ecological impacts, and decision tradeoffs. *Environmental Management*, *44*, 921–927.

Larson, K.L., White, D.D., Gober, P., Harlan, S., & Wutich, A. (2009b). Divergent perspectives on water resource sustainability in a public–policy–science context. *Environmental Science & Policy*, *12*, 1012–1023.

Li, J., Song, C., Cao, L., Meng, X., & Wu, J. (2011). Impacts of landscape structure on surface urban heat islands: A case study of Shanghai, China. *Remote Sensing of Environment*, *115*, 3249–3263.

Li, J., Wang, Y., Shen, X., & Song, Y. (2004). Landscape pattern analysis along an urban–rural gradient in the Shanghai metropolitan region. *Acta Ecologica Sinica*, *24*, 1973–1980.

Li, W., Goodchild, M.F., & Church, R. (2013a). An efficient measure of compactness for two-dimensional shapes and its application in regionalization problems. *International Journal of Geographical Information Science*, *27*, 1227–1250.

Li, Z. -L., Tang, B. -H., Wu, H., Ren, H., Yan, G., Wan, Z., ... Sobrino, J.A. (2013b). Satellite-derived land surface temperature: Current status and perspectives. *Remote Sensing of Environment*, *131*, 14–37.

Li, W., Church, R.L., & Goodchild, M.F. (2014a). The p-compact-regions problem. *Geographical Analysis*, *46*(3), 250–273.

Li, X., Myint, S.W., Zhang, Y., Galletti, C., Zhang, X., & Turner, B.L., II (2014b). Object-based land-cover classification for metropolitan phoenix, Arizona, using aerial photography. *International Journal of Applied Earth Observation and Geoinformation*, *33*, 321–330.

Li, X., Zhou, W., Quyang, W., & Zheng, H. (2012). Spatial pattern of greenspace affects land surface temperature: Evidence from the heavily urbanized Beijing metropolitan area China. *Landscape Ecology*, *27*, 887–898.

Lichstein, J.W., Simons, T.R., Shriner, S.A., & Franzreb, K.E. (2002). Spatial autocorrelation and autoregressive models in ecology. *Ecological Monographs*, *72*, 445–463.

Liu, L., & Zhang, Y. (2011). Urban heat island analysis using the Landsat TM data and ASTER data: A case study in Hong Kong. *Remote Sensing*, *3*(7), 1535–1552.

Lo, C.P., Qiattrochi, D.A., & Luvall, J.C. (1997). Application of high-resolution thermal infrared remote sensing and GIS to assess the urban heat island effect. *International Journal of Remote Sensing*, *18*, 287–304.

Maimaitiyiming, M., Ghulum, A., Tiyip, T., Pia, F., Latorre-Camona, P., Halik, U., ... Caetano, M. (2014). Effects of green space spatial pattern on land surface temperature: Implications for sustainable urban planning and climate change adaptation. *ISPRS Journal of Photogrammetry and Remote Sensing*, *89*, 59–66.

Markham, B.L., & Barker, J.L. (1985). Spectral characterization of the LANDSAT thematic mapper sensors. *International Journal of Remote Sensing*, *6*, 697–716.

Martin, C.A. (2008). *Landscape sustainability in a Sonoran desert city. Cities and the environment 1, article 5.*

McGarigal, K., & Marks, B.J. (1995). Spatial pattern analysis program for quantifying landscape structure. *Gen. Tech. Rep. PNW-GTR-351. US Department of Agriculture*. Forest Service, Pacific Northwest Research Station.

McGarigal, K., Cushman, S.A., & Ene, E. (2012). *FRAGSTATS v4: Spatial pattern analysis program for categorical and continuous maps.* Amherst, MA: University of Massachusettes (URL http://www. umass. edu/landeco/research/fragstats/fragstats. html).

Middel, A., Brazel, A.J., Kaplan, S., & Myint, S. (2012). Daytime cooling efficiency and diurnal energy balance in Phoenix, Arizona, USA. *Climate Research*, *54*, 21–34.

Middel, A., Häb, K., Brazel, A.J., Martin, C.A., & Guhathakurta, S. (2014). Impact of urban form and design on mid-afternoon microclimate in Phoenix local climate zones. *Landscape and Urban Planning*, *122*, 16–28.

Miller, V.C. (1953). *A quantitative geomorphic study of drainage basin characteristics in the Clinch mountain area.* New York: Department of Geology, Columbia University.

Mitraka, Z., Berger, M., Ruescas, A., Sobrino, J.A., Jiménez-Muñoz, J.C., Brockmann, C., & Chrysoulakis, N. (2013). Estimation of land surface emissivity and temperature based on spatial–spectral unmixing analysis. *In 3rd ME- RIS/(A)ATSR & OCLI-SLSTR preparatory workshop, Frascati, Italy* (pp. 15–19) (October 2013).

Myint, S.W., Wentz, E.A., Brazel, A.J., & Quattrochi, D.A. (2013). The impact of distinct anthropogenic and vegetation features on urban warming. *Landscape Ecology*, *28*, 959–978.

Nichol, J.E. (1996). High-resolution surface temperature patterns related to urban morphology in a tropical city: A satellite based study. *Journal of Applied Meteorology*, *35*, 135–146.

Oke, T.R. (1976). The distinction between canopy and boundary layer heat islands. *Atmosphere*, *14*, 268–277.

Oke, T.R. (1982). The energetic basis of the urban heat island. *Quarterly Journal of the Royal Meteorological Society*, *108*, 1–24.

Oke, T.R. (1997). Urban climates and global change. In A. Perry, & R. Thompson (Eds.), *Applied climatology: Principles and practices* (pp. 273–287) (London, Routledge, London).

Rizwan, A.M., Dennis, L.Y.C., & Liu, C. (2008). A review on the generation, determination and mitigation of Urban Heat Island. *Journal of Environmental Sciences*, *20*, 120–128.

Rozenstein, O., Qin, Z., Derimian, Y., & Karnieli, A. (2014). Derivation of land surface temperature for Landsat-8 TIRS using a split window algorithm. *Sensors*, *14*, 5768–5780 (Basel, Switzerland).

Sailor, D.J. (1995). Simulated urban climate response to modifications in surface albedo and vegetative cover. *Journal of Applied Meteorology*, *34*, 1694–1704.

Saunders, S.C., Chen, J.Q., Crow, T.R., & Brosofske, K.D. (1998). Hierarchical relationships between landscape structure and temperature in a managed forest landscape. *Landscape Ecology*, *13*, 381–395.

Schwartzberg, J.E. (1965). Reapportionment, gerrymanders, and the notion of compactness. *Minnesota Law Review*, *50*, 443.

Sha, M., & Tian, G. (2010). An analysis of spatiotemporal changes of urban landscape pattern in Phoenix metropolitan region. *Procedia Environmental Sciences*, *2*, 600–604.

Shrestha, M.K., York, A.M., Boone, C.G., & Zhang, S. (2012). Land fragmentation due to rapid urbanization in the phoenix metropolitan area: analyzing the spatiotemporal patterns and drivers. *Applied Geography*, *32*, 522–531.

Smith, D.L., & Johnson, L. (2004). Vegetation-mediated changes in microclimate reduce soil respiration as woodlands expand into grasslands. *Ecology*, *85*, 3348–3361.

Snyder, W.C., Wan, Z., Zhang, Y., & Feng, Y.Z. (1998). Classification-based emissivity for land surface temperature measurement from space. *International Journal of Remote Sensing*, *19*, 2753–2774.

Sobrino, J.A., Bianchi, R., Paganini, M., Soria, G., Jimenez-Munzos, J., Oltra-Cario, R., et al. (2009). *Dual-use European security IR experiment 2008 (DESIREX 2008).* Frascati (Italy), European Space Agency (ESA): Final Report.

Sobrino, J.A., Caselles, V., & Becker, F. (1990). Significance of the remotely sensed thermal infrared measurements obtained over a citrus orchard ISPRS. *Photogrammetric Engineering and Remote Sensing*, *44*, 343–354.

Sobrino, J.A., Jiménez-Muñoz, J.C., Sòria, G., Romaguera, M., Guanter, L., Moreno, J., ... Martínez, P. (2008). Land surface emissivity retrieval from different VNIR and TIR sensors. *IEEE Transactions on Geoscience and Remote Sensing*, *46*, 316–327.

Sobrino, J.A., Jimenez-Munoz, J.C., & Paolini, L. (2004). Land surface temperature retrieval from LANDSAT TM 5. *Remote Sensing of Environment*, *90*, 434–440.

Stabler, L.B., Martin, C.A., & Brazel, A.J. (2005). Microclimates in a desert city were related to land use and vegetation index. *Urban Forestry & Urban Greening*, *3*, 137–147.

Stone, B., Jr. (2007). Urban sprawl and air quality in large US cities. *Journal of Environmental Management*, *86*, 688–698.

Stone, B., Jr., & Rodgers, M.O. (2001). Urban form and thermal efficiency: How the design of cities influences the urban heat island effect. *Journal of the American Planning Association*, *67*, 186–198.

Streutker, D.R. (2002). A remote sensing study of the Urban Heat Island of Houston, Texas. *International Journal of Remote Sensing*, *23*, 2592–2608.

Turner, B.L., II, Janetos, A.C., Verburg, P.H., & Murray, A.T. (2013). Land system architecture: Using land systems to adapt and mitigate global environmental change. *Global Environmental Change*, *23*, 395–397.

Turner, V.K., & Ibes, D.C. (2011). The impact of homeowners associations on residential water demand management in Phoenix, Arizona. *Urban Geography*, *32*, 1167–1188.

Unger, J. (2004). Intra-urban relationship between surface geometry and urban heat island: Review and new approach. *Climate Research*, *27*, 253–264.

Vanos, J.K., Middel, A., McKercher, G.R., Kuras, E.R., & Ruddell, B.L. (2015). *Multiscale surface temperature analysis of urban playgrounds in a hot, dry city. Landscape and urban planning.* (inpress).

Weng, Q., & Fu, P. (2014). Modeling annual parameters of clear-sky land surface temperature variations and evaluating the impact of cloud cover using time series of Landsat TIR data. *Remote Sensing of Environment*, *140*, 267–278.

Weng, Q., Lu, D., & Schubring, J. (2004). Estimation of land surface temperature–vegetation abundance relationship for Urban Heat Island studies. *Remote Sensing of Environment*, *89*, 467–483.

Xian, G., & Crane, M. (2006). An analysis of urban thermal characteristics and associated land cover in Tampa Bay and Las Vegas using Landsat satellite data. *Remote Sensing of Environment*, *104*, 147–156.

Yu, X., Guo, X., & Wu, Z. (2014). Land surface temperature retrieval from Landsat 8 tirs—comparison between radiative transfer equation-based method, split window algorithm and single channel method. *Remote Sensing*, *6*, 9829–9852.

Zhang, X., Zhong, T., Feng, X., & Wang, K. (2009). Estimation of the relationship between vegetation patches and urban land surface temperature with remote sensing. *International Journal of Remote Sensing*, *30*, 2105–2118.

Zhang, Y., Odeh, I.O.A., & Ramadan, E. (2013). Assessment of land surface temperature in relation to landscape metrics and fractal vegetation cover in an urban/peri-urban region using Landsat data. *International Journal of Remote Sensing*, *34*, 168–189.

Zheng, B., Myint, S.W., & Fan, C. (2014). Spatial configuration of anthropogenic land cover impacts on urban warming. *Landscape and Urban Planning*, *130*, 104–111.

Zhou, W., Huang, G., & Cadensasso, M.L. (2011). Does spatial configuration matter? Understanding the effects of land cover pattern on land surface temperature in urban landscapes. *Landscape and Urban Planning*, *102*, 54–63.

Zhou, W., Qian, Y., Li, X., Li, W., & Han, L. (2014). Relationships between land cover and the surface urban heat island: seasonal variability and effects of spatial and thematic resolution of land cover data on predicting land surface temperatures. *Landscape Ecology*, *29*, 153–167.